Phase-field simulations of intergranular fission gas bubble behavior in U_3Si_2 nuclear fuel

Larry K. Aagesen[a,*], David Andersson[b], Benjamin W. Beeler[c], Michael W. D. Cooper[b], Kyle A. Gamble[a], Yinbin Miao[d], Giovanni Pastore[a], Michael R. Tonks[e]

[a] *Computational Mechanics and Materials Department, Idaho National Laboratory, P.O. Box 1625, Idaho Falls, ID 83415, USA*
[b] *Materials Science and Technology Division, Los Alamos National Laboratory, P.O. Box 1663, Los Alamos, NM, 87545, USA*
[c] *Department of Nuclear Engineering, North Carolina State University, Raleigh, NC, 27695, USA*
[d] *Argonne National Laboratory, Lemont, IL, 60439, USA*
[e] *Department of Materials Science and Engineering, University of Florida, P.O. Box 116400, Gainesville, FL 32611, USA*

Abstract

U_3Si_2 is a potential accident-tolerant fuel that shows promise due to its high thermal conductivity and higher uranium density relative to UO_2. However, its swelling and fission gas release behavior in light water reactor (LWR) conditions is relatively unknown. To provide mechanistic insight and determine parameters for engineering-scale fuel performance modeling of pellet-form U_3Si_2, phase-field simulations of the growth, interconnection, and venting of intergranular fission gas bubbles were performed. The fractional coverage of the grain boundary and the fraction of bubble area that is vented was calculated as a function of time. From the simulation data, the fractional grain boundary coverage at saturation, an important parameter needed in engineering-scale modeling of swelling and fission gas release, was determined. Multiple simulations were run to determine the uncertainty in the calculated value. The effect of model assumptions and input parameters that are not well known was evaluated. Based on the simulation results, a value of 0.60 for the fractional grain boundary coverage at saturation is recommended for U_3Si_2 fuel.

*Corresponding Author. Email: Larry.Aagesen@inl.gov.

Keywords: phase-field, fission gas, uranium silicide, accident tolerant fuel

1. Introduction

In recent years, the desire for commercial nuclear reactor fuels that are more tolerant of accident conditions has driven research into alternatives to the UO_2 pellets clad in Zircaloy that are currently used in light water reactors (LWRs). One promising candidate for accident-tolerant fuel (ATF) applications is U_3Si_2, due to its higher thermal conductivity compared to UO_2 [1]. Although U_3Si_2's melting temperature is lower than that of UO_2, its much higher thermal conductivity results in greater margin to the melting temperature in both normal operation and accident conditions [2, 3].

Despite these potential advantages, the swelling behavior of U_3Si_2 remains poorly understood. Past experience with dispersion-form U_3Si_2 fuel in research reactors [4] has indicated that swelling could be a significant issue in U_3Si_2; however, it is unknown whether swelling in dispersion fuel in research reactors is representative of swelling that would be encountered in pellet-form fuel at the higher temperatures typical of commercial LWRs. Dispersion-form U_3Si_2 undergoes fission-induced amorphization [4], which may strongly influence swelling. However, the much higher operating temperatures of pellet-form fuel in LWRs may prevent fission-induced amorphization [5–9]; based on experimental observations, U_3Si_2 is crystalline under irradiation for temperatures of 350 °C and above [5], and simulations with the fuel performance code BISON show that temperature throughout a U_3Si_2 LWR pellet remains above 350 °C throughout fuel lifetime during steady-state operation [3]. Thus, given the expected lack of amorphization in U_3Si_2 LWR fuel, the mechanism of swelling may be different from research reactors. The only data extant on pellet-form U_3Si_2 indicates that swelling could be greater than 10% for a low burnup of 0.65% fissions per initial metal atom (FIMA) [10].

To provide predictive capability for the performance of U_3Si_2 nuclear fuel, several computational modeling approaches have been employed. Rest devel-

oped a model for the behavior of U_3Si_2 under conditions typical of research reactors, where amorphization of U_3Si_2 would be be expected to occur [11]. Miao et al. parameterized a rate theory model for fission gas behavior and applied it to study swelling of U_3Si_2 in LWRs [2, 3]. Barani et al. recently developed a model for U_3Si_2 fission gas behavior in LWRs [12], implemented within Idaho National Laboratory's BISON fuel performance code. The model tracks the populations of intragranular and intergranular bubbles. It assumes that, similar to UO_2 fuel, fission gas atoms can be trapped in intragranular bubbles and subsequently re-solved back into the matrix due to impacts by energetic fission fragments. The balance between trapping and re-solution affects the rate of transport of fission gas atoms to grain boundaries. Also similar to UO_2, the model assumes that fission gas release from the fuel is controlled by the grain boundary (intergranular) bubbles. This is based on experimental observations of U_3Si_2 irradiated at LWR temperatures [10], which showed the presence of intergranular bubbles with sizes comparable to those observed in UO_2.The model tracks the number density and size of the bubbles and calculates the fractional coverage of the grain boundaries until the onset of gas release at the attainment of a saturation coverage value, based on the approach of Ref. [13].

In Ref. [12], a sensitivity analysis was carried out to determine the model parameters that most strongly influence swelling and fission gas release (FGR). Two parameters that had a strong impact on the predictions of these quantities were the surface energy between the fuel matrix and intergranular bubbles, σ_{mb}, and the intergranular bubbles' dihedral angle θ, which is determined by the balance of surface energy and grain boundary energy. Improved estimates for these parameters were recently developed based on [14] as $\sigma_{mb} = 1.7$ J/m^2 and $\theta = 146°$. Another parameter that strongly affected swelling and FGR was the saturation coverage of grain boundaries, $F_{c,sat}$. In the model, the fractional coverage of the grain boundaries by intergranular bubbles, F_c, is tracked and increases as the bubbles grow and coalesce until it reaches $F_{c,sat}$. At that point, it is assumed that the bubbles interconnect to form a percolated network across the grain boundary, and that a free path exists from interior grain boundaries

to free surfaces of the pellet (possibly through a network of tunnels that forms along the triple junctions in the grain structure [15]). Therefore, the model assumes that when $F_c = F_{c,sat}$ at a particular location, all gas contained in the intergranular bubbles at that location is released to the free space between the fuel and cladding. From that point on, F_c does not increase past $F_{c,sat}$, and any fission gas reaching the grain boundaries at that location is immediately transported to the free space between the fuel and cladding.

Based on experimental observations of intergranular bubbles [16], a value of $F_{c,sat} = 0.5$ has been used for simulations of swelling and FGR in UO_2 [13, 17]. However, to our knowledge there is insufficient experimental evidence to determine $F_{c,sat}$ for U_3Si_2 fuel at LWR operating temperatures. For this reason, in Ref. [12], the theoretical value for saturation coverage by a uniform square lattice, $F_{c,sat} = 0.78$, was used [18].

In past work, phase-field simulations were used to investigate the process of growth, interconnection, and venting of grain boundary bubbles in UO_2 [19]. In that work, the phase-field model included the effects of surface and grain boundary energies to capture the bubble morphology correctly. Bubble growth was driven by supersaturation of fission gas atoms in the fuel matrix surrounding the bubbles; thus, the simulation conditions were more representative of post-irradiation annealing than normal operation. Ref. [19] investigated the rate at which the bubbles vented to a triple junction network that was assumed to exist at the periphery of the simulation domain. It was found that two of the most important factors controlling the rate at which bubbles vented were the bubble dihedral angle and the areal density of the bubbles.

In this work, we employ an approach similar to Ref. [19] to investigate the progress toward venting of grain boundary bubbles in U_3Si_2, and use the phase-field simulation results to determine a value for $F_{c,sat}$ for U_3Si_2 to be used in the fission gas release model described in Ref. [12]. We employ a phase-field model implemented within Marmot, Idaho National Laboratory's mesoscale simulation code [20]. The model in the present work incorporates additional physics beyond the model used in Ref. [19], including tracking of both vacancy and fission gas

defect species, dependence of the bulk free energy density on these defect species concentrations, and source terms for the production of these defect species at normal LWR operating conditions. The model was originally presented and parametrized for UO_2 in Ref. [15]. Here, the model is parametrized for U_3Si_2 using atomistic and rate theory simulation results. The remainder of this work is organized as follows. In Section 2, the phase-field model formulation and parametrization is described. In Section 3, the simulation results are presented and analyzed to determine $F_{c,sat}$ for U_3Si_2, and the uncertainties associated with the model and with input parameters that are not well known are determined. Finally, in Section 4, conclusions are drawn and directions for future work are suggested.

2. Model formulation and parametrization

The phase-field model used to simulate the evolution of the intergranular bubbles was originally described in Ref. [15]. Key features of the model and parametrization for U_3Si_2 are given in the remainder of this section. The microstructure of the fuel consists of multiple grains of U_3Si_2 and intergranular fission gas bubbles. In the phase-field model, the microstructure is represented with a set of order parameters. For a microstructure consisting of p grains, the individual grains of the fuel matrix are represented by a set of order parameters $\eta_{m1}, \eta_{m2}, \ldots, \eta_{mp}$. Each fission gas bubble is crystallographically indistinguishable from the others, so the bubbles are represented by a single order parameter η_{b0}. Within the interior of grain i of the fuel, $\eta_{mi} = 1$, $\eta_{mj} = 0\ \forall j \neq i$, and $\eta_{b0} = 0$. Within the bubble phase, $\eta_{b0} = 1$ and $\eta_{mj} = 0\ \forall j$. Interfaces between grains are represented by a smooth variation of the order parameters.

In addition to the local crystal structure, the local concentration of defect species is also used to describe the microstructure. In the present model, we assume that the dominant defect species are U vacancies and fission gas atoms on U lattice sites. Both U vacancies and interstitials are produced by collision cascades; however, interstitials are much more mobile and therefore diffuse to

sinks much more rapidly than vacancies. Therefore, there is a net formation of vacancies which can be represented by a source term for net vacancy production. For fission gas atoms on U lattice sites, the formation of bubbles is driven by the low-solubility Xe and Kr atoms. We assume that the properties of all insoluble fission gas atoms can be described by the properties of Xe atoms on U sites, since Xe production occurs at a rate nearly ten times that of Kr [21]. The density of vacancies and gas atoms are represented by variables ρ_v and ρ_g, respectively, with units of number of defects per unit volume. These quantities can be converted to the local composition (mole fraction) c of the U lattice using $c = \rho V_a$, where V_a is the atomic volume occupied by a U atom in the U_3Si_2 crystal structure. V_a was calculated to be 0.0363 nm^3 by dividing the unit cell volume of 0.218 nm^3 (calculated from experimental data [1]) by 6 U atoms in the unit cell.

2.1. Grand potential functional

To derive the evolution equations for the microstructure, the total grand potential Ω of the system is written as a function of the local grand potential density:

$$\Omega = \int_V \left(m \left[\sum_\alpha \sum_{i=1}^{p_\alpha} \left(\frac{\eta_{\alpha i}^4}{4} - \frac{\eta_{\alpha i}^2}{2} \right) + \sum_\alpha \sum_{i=1}^{p_\alpha} \left(\sum_\beta \sum_{j=1, \alpha i \neq \beta j}^{p_\beta} \frac{\gamma_{\alpha i \beta j}}{2} \eta_{\alpha i}^2 \eta_{\beta j}^2 \right) + \frac{1}{4} \right] + \frac{\kappa}{2} \sum_\alpha \sum_{i=1}^{p_\alpha} |\nabla \eta_{\alpha i}|^2 + \sum_\alpha h_\alpha \omega_\alpha \right) dV \tag{1}$$

where α and β are indices for phases, i and j are indices for grains of each phase, p_α and p_β are the number of grains of phase α and β, m is a constant free energy barrier coefficient, κ is the gradient energy coefficient (considered to be independent of interface orientation and misinclination here), and the set of constant coefficients $\gamma_{\alpha i \beta j}$ allow the adjustment of interfacial energies between phases and grains. ω_α is the local grand potential density of each phase, and h_α is a switching function for phase α that has value $h_\alpha = 1$ in phase α and $h_\alpha = 0$

in all other phases. In Eq. (1), the first and second terms ensure that a minimum in the free energy exists within the interior of each grain, and contribute to the interfacial energies between different phases/grains. The third term ($\frac{m}{4}$) is added to make the homogeneous free energy density equal to 0 within grain interiors. The fourth term penalizes gradients in the order parameters representing each grain and also contributes to the interfacial energies between different grains/phases. The fifth term adds the appropriate grand potential density for each phase. The switching function used to interpolate the grand potential densities was introduced in Ref. [22] and has the form

$$h_\alpha = \frac{\sum_{i=1}^{p_\alpha} \eta_{\alpha i}^2}{\sum_\beta \sum_{i=1}^{p_\beta} \eta_{\beta i}^2} \tag{2}$$

For the matrix and bubble phases, the switching functions reduce to

$$h_m = \frac{\sum_{i=1}^{p} \eta_{mi}^2}{\eta_{b0} + \sum_{i=1}^{p} \eta_{mi}^2} \tag{3}$$

$$h_b = \frac{\eta_{b0}}{\eta_{b0} + \sum_{i=1}^{p} \eta_{mi}^2} \tag{4}$$

The grand potential density for each phase is given by

$$\omega_m = f_m - \mu_g \rho_g - \mu_v \rho_v \tag{5}$$

$$\omega_b = f_b - \mu_g \rho_g - \mu_v \rho_v \tag{6}$$

where f_m and f_b are the Helmholtz free energies of each phase and μ_g and μ_v are the chemical potentials of the gas atoms and vacancies, respectively. The Helmholtz free energies are given by

$$f_m = f_{m,chem} \tag{7}$$

$$f_b = f_{b,chem} \tag{8}$$

where $f_{m,chem}$ and $f_{b,chem}$ are the chemical energy contributions. As in Ref. [15], the bubbles are assumed to have gas pressure at the equilibrium pressure for

their size as determined by the Laplace-Young equation; thus, the surface tension of the bubble-matrix interface balances the gas bubble pressure and no stress is exerted by the bubbles on the surrounding fuel matrix. Therefore, no contribution to the Helmholtz free energy due to elastic deformation is included.

2.2. Chemical energy contribution and parameterization

Using the ideal solution model, the Helmholtz free energy density is written

$$\begin{aligned} f_{m,ideal} = \frac{1}{V_m}\big\{ & RT[c_v \ln c_v + (1-c_v)\ln(1-c_v)] + N_A E_v^f c_v \\ & + RT[c_g \ln c_g + (1-c_g)\ln(1-c_g)] + N_A E_g^f c_g \big\} \end{aligned} \tag{9}$$

where V_m is the molar volume, R is the ideal gas constant, $V_m = V_a N_A$, N_A is Avogadro's number, E_v^f is the formation energy of a U vacancy, and E_g^f is the formation (solution) energy of a gas (Xe) atom on a U lattice site, and T is the temperature (assumed to be 1035 K, representative of temperature at the fuel centerline during high power LWR conditions). As determined from DFT calculations [23], $E_v^f = 1.69$ eV and $E_g^f = 4.92$ eV. To simplify the numerical solution of the governing equations, $f_{m,ideal}$ was approximated with a parabolic function:

$$f_{m,chem} = \frac{1}{2}k_v^m (c_v - c_v^{m,eq})^2 + \frac{1}{2}k_g^m (c_g - c_g^{m,eq})^2 \tag{10}$$

where k_v^m and k_g^m are the curvatures of the parabolas and $c_v^{m,eq}$ and $c_g^{m,eq}$ are the equilibrium composition of vacancies and gas atoms in the U_3Si_2 matrix. The equilibrium compositions are determined from the formation energies and temperature using $c_v^{m,eq} = \exp(-E_v^f/k_BT)$ and $c_g^{m,eq} = \exp(-E_g^f/k_BT)$. The curvatures of the parabolas are set by assuming that when the vacancy composition, c_v, is equal to the steady-state vacancy composition during reactor operation, c_v^0, the chemical potential determined from the parabolic approximation is equal to the chemical potential of the ideal solution model, as originally described in Ref. [24]. Since $\mu = \frac{\partial f}{\partial \rho} = \frac{\partial f}{\partial c}\frac{\partial c}{\partial \rho} = V_a \frac{\partial f}{\partial c}$,

$$V_a \frac{\partial f_{m,chem}}{\partial c_v}\bigg|_{c_v^0} = V_a \frac{\partial f_{m,ideal}}{\partial c_v}\bigg|_{c_v^0} \tag{11}$$

This leads to an expression for k_v^m, assuming $c_v^0 = 5 \times 10^{-3}$:

$$k_v^m = \frac{1}{(c_v^0 - c_v^{m,eq})} \left[\frac{RT}{V_m} [\ln c_v^0 - \ln (1 - c_v^0)] + \frac{N_A E_v^f}{V_m} \right] = 5.38 \times 10^{11} \text{ J/m}^3 \quad (12)$$

For simplicity, it is assumed that $k_g^m = k_v^m$.

The bulk chemical free energy density of the gas bubble phase, $f_{b,chem}$, is determined by considering the gas phase to be a mixture of U-site vacancies and Xe atoms as described in Ref. [15]. It is assumed that the van der Waals gas equation of state applies to Xe [21], in which the gas atoms are assumed to have a hard-sphere exclusion volume characterized by the parameter b, and we neglect long-range interactions due to the high density of gas in the bubbles. For Xe, $b = 0.085$ nm^3/atom [21]. With these assumptions, the Helmholtz free energy density of the gas is [25]:

$$f_{b,vdW} = n_g kT \left[\ln \left(\frac{1}{n_Q \left(\frac{1}{n_g} - b \right)} \right) - 1 \right] + f_0 \quad (13)$$

where n_g is the number density of gas atoms, $n_Q = \left(\frac{m k_B T}{2\pi\hbar} \right)^{3/2}$ is the quantum concentration, m is the mass of a Xe atom, and f_0 is the offset to ensure that the solid and gas free energies are measured relative to the same reference state. n_g can be put in terms of the model variables using $n_g = c_g n_U$ (where $n_U = 1/V_a$ is the number density of U atoms in the U_3Si_2 lattice) as long as $c_v + c_g = 1$ holds. f_0 is determined by setting the minima of the gas and solid phase free energies equal to each other, resulting in $f_0 = 1.82 \times 10^9$ J/m^3.

To simplify numerical calculations, a parabolic approximation was also fit to the Helmholtz free energy of the gas phase:

$$f_{b,chem} = \frac{1}{2} k_v^b (c_v - c_v^{b,eq})^2 + \frac{1}{2} k_g^b (c_g - c_g^{b,eq})^2 \quad (14)$$

The minimum of the parabolic free energy was set to occur at the minimum of the van der Waals free energy, resulting in $c_g^{b,eq} = 0.3924$ and $c_v^{b,eq} = 0.6076$. Because composition in the gas bubbles will generally not deviate far from the minimum of the free energy, k_v^b and k_g^b were set by assuming $k_v^b = k_g^b$ and fitting to $f_{b,vdW}$ in the range $0.36 < c_g < 0.42$, resulting in $k_v^b = k_g^b = 8.0 \times 10^{10}$ J/m^3.

2.3. Interfacial energy and parameterization

Based on the results of Ref. [14], the interfacial energy between the matrix and gas bubble phase was calculated to be $\sigma_{mb} = 1.7$ J/m^2. Although a range of energies was calculated for different grain boundaries in Ref. [14], the current BISON model for fission gas release only considers a single dihedral angle for intergranular bubles. Therefore, for the purposes of the present work, a single representative grain boundary energy was chosen to be $\sigma_{mm} = 1.0$ J/m^2. For an intergranular bubble, this results in a dihedral angle of 146°. In this section, the process of choosing phase-field model parameters to accurately include these interfacial and grain boundary energies is described.

Using the grand potential functional of Eq. (1), the interfacial energy $\sigma_{\alpha i \beta j}$ between grain i of phase α and grain j of phase β is given by [22, 26]

$$\sigma_{\alpha i \beta j} = g(\gamma_{\alpha i \beta j})\sqrt{\kappa m} \tag{15}$$

where $g(\gamma_{\alpha i \beta j})$ is a dimensionless function of γ that in general must be evaluated numerically. However, for the special case $\gamma = 1.5$, $g(\gamma = 1.5) = \sqrt{2}/3$. For this special case, analytical expressions can be used that relate κ and m to the interfacial energy and characteristic thickness l_{int} of the interface [22, 26]:

$$\kappa = \frac{3}{4}\sigma_{mb} l_{int} \tag{16}$$

$$m = \frac{6\sigma_{mb}}{l_{int}} \tag{17}$$

To resolve the intergranular bubbles, l_{int} is chosen to be 30 nm, and we choose the interface between any grain i of the matrix phase and the bubble phase to have $\gamma_{mib0} = 1.5$, resulting in $\kappa = 1.92 \times 10^{-8}$ J/m and $m = 6.84 \times 10^8$ J/m^3. To control the grain boundary energies, since κ and m are fixed, the parameters γ_{mimj} must be determined to obtain the correct value of σ_{mm}, which is assumed to be constant and isotropic for all interfaces between grains i and j. To determine the value of γ_{mimj}, using Eq. (15),

$$\sigma_{mb} = g(\gamma_{mib0})\sqrt{\kappa m} \tag{18}$$

$$\sigma_{mm} = g(\gamma_{mimj})\sqrt{\kappa m} \tag{19}$$

Dividing Eq. (18) by Eq. (19),

$$\frac{\sigma_{mb}}{\sigma_{mm}} = \frac{g(\gamma_{mib0})}{g(\gamma_{mimj})} \tag{20}$$

Rearranging Eq. (20),

$$g(\gamma_{mimj}) = g(\gamma_{mib0} = 1.5)\frac{\sigma_{mm}}{\sigma_{mb}} = \frac{\sqrt{2}}{3}\frac{1.0}{1.7} = 0.27 \tag{21}$$

A polynomial approximation has been fit to numerical results that allows γ to be found as a function of g [27]:

$$\gamma = \left(-5.288g^8 - 0.09364g^6 + 9.965g^4 - 8.813g^2 + 2.007\right)^{-1} \tag{22}$$

Using this approximation, $\gamma_{mimj} = 0.67$.

2.4. Evolution equations

From the grand potential functional of Eq. (1), the Allen-Cahn equations for evolution of the order parameters can be derived:

$$\begin{aligned}
\frac{\partial \eta_{\alpha i}}{\partial t} &= -L\frac{\delta \Omega}{\delta \eta_{\alpha i}} \\
\frac{\partial \eta_{\alpha i}}{\partial t} &= -L\left[m\left(\eta_{\alpha i}^3 - \eta_{\alpha i} + 2\eta_{\alpha i}\sum_{\beta}\sum_{j=1,\alpha i\neq\beta j}^{p_\beta}\gamma_{\alpha i\beta j}\eta_{\beta j}^2\right)\right. \\
&\qquad \left. - \kappa\nabla^2\eta_{\alpha i} + \sum_{\alpha}\frac{\partial h_\alpha}{\partial \eta_{\alpha i}}\omega_\alpha\right]
\end{aligned} \tag{23}$$

where $\frac{\delta\Omega}{\delta\eta_{\alpha i}}$ is the variational derivative of Ω with respect to order parameter $\eta_{\alpha i}$ and L is the order parameter mobility, which in general is a function of order parameters and concentration. Parameterization of L will be discussed later in this section.

To evolve the gas and vacancy concentrations, it is more convenient to write the evolution equations in terms of chemical potentials μ_v and μ_g and use the chemical potentials as the field variables rather than densities. To enable this,

the grand potentials in each phase, Eq. (5) - (6), must be expressed in terms of μ_v and μ_g. For the matrix phase, the relation $\mu_g = V_a \frac{\partial f_{m,chem}}{\partial c_g} = V_a k_g^m (c_g - c_g^{m,eq})$ can be re-arranged to yield

$$c_g = \frac{\mu_g}{V_a k_g^m} + c_g^{m,eq} \tag{24}$$

Similarly,

$$c_v = \frac{\mu_v}{V_a k_v^m} + c_v^{m,eq} \tag{25}$$

Eq. (24) - (25) can be used in conjunction with the relations $\rho_g = \frac{c_g}{V_a}$, $\rho_v = \frac{c_v}{V_a}$, Eq. (5), (7), and (10) to obtain the grand potential density as a function of chemical potentials rather than concentrations:

$$\omega_m = -\frac{1}{2}\frac{\mu_v^2}{V_a^2 k_v^m} - \frac{\mu_v}{V_a} c_v^{m,eq} - \frac{1}{2}\frac{\mu_g^2}{V_a^2 k_g^m} - \frac{\mu_g}{V_a} c_g^{m,eq} \tag{26}$$

Similarly, the grand potential density of the bubble phase can be expressed as

$$\omega_b = -\frac{1}{2}\frac{\mu_v^2}{V_a^2 k_v^b} - \frac{\mu_v}{V_a} c_v^{b,eq} - \frac{1}{2}\frac{\mu_g^2}{V_a^2 k_g^b} - \frac{\mu_g}{V_a} c_g^{b,eq} \tag{27}$$

The evolution equations for μ_g and μ_v are

$$\frac{\partial \mu_g}{\partial t} = \frac{1}{\chi_g}\left[\nabla \cdot (D_g \chi_g \nabla \mu_g) + s_g - \sum_\alpha \sum_{i=1}^{p_\alpha} \frac{\partial \rho_g}{\partial \eta_{\alpha i}} \frac{\partial \eta_{\alpha i}}{\partial t}\right] \tag{28}$$

$$\frac{\partial \mu_v}{\partial t} = \frac{1}{\chi_v}\left[\nabla \cdot (D_v \chi_v \nabla \mu_v) + s_v - \sum_\alpha \sum_{i=1}^{p_\alpha} \frac{\partial \rho_v}{\partial \eta_{\alpha i}} \frac{\partial \eta_{\alpha i}}{\partial t}\right] \tag{29}$$

where χ_g and χ_v are the susceptibilities as defined later in this section, D_g and D_v are the diffusion coefficients, and s_g and s_v are the source terms for production of Xe atoms and U site vacancies.

The source term $s_g = s_g^0 h_m$ is given by a constant rate of Xe production, s_g^0, times the switching function h_m, which has a value of 1 in the fuel matrix and zero inside the bubble. This is to limit production of new Xe atoms to the fuel matrix in the model. The Xe production rate $s_g^0 = \dot{F} Y_{Xe}$, where $\dot{F}$ is the fission rate density and Y_{Xe} is the fission yield of Xe. $\dot{F}$ is estimated to be 1.26×10^{13} fissions/(cm^3 s) based on typical operating values for a light water reactor [21], scaled up to account for the increased U site density of U_3Si_2 compared with

UO_2. Y_{Xe} is taken to be 0.2156 based on the thermal neutron Xe yield for U-235 [28]. The vacancy production rate is similarly given by $s_v = s_v^0 h_m$. s_v^0 has not been determined to our knowledge, so we assume a value of $s_v^0 = 10 s_g^0$.

The susceptibility χ describes the relationship between solute density and its chemical potential: $\chi = \frac{\partial \rho}{\partial \mu}$ [29]. This relationship differs based on the phase of the system, so χ is interpolated based on the local phase using the switching functions h_α. For gas atoms,

$$\chi_g = h_m \chi_g^m + h_b \chi_g^b \tag{30}$$

where $\chi_g^m = \frac{\partial \rho_g^m}{\partial \mu_g}$ and $\chi_g^b = \frac{\partial \rho_g^b}{\partial \mu_g}$. Since the governing equations are in terms of the chemical potentials, the susceptibilities must also be expressed in terms of chemical potentials, which can be done as follows. Using $\rho_g^m = \frac{c_g}{V_a}$, and substituting for c_g using Eq. (24), $\chi_g^m = \frac{\partial \rho_g^m}{\partial \mu_g} = \frac{1}{V_a^2 k_g^m}$. Similar expressions can be derived for χ_v^m, χ_g^b, and χ_v^b, resulting in

$$\chi_g = h_m \frac{1}{V_a^2 k_g^m} + h_b \frac{1}{V_a^2 k_g^b} \tag{31}$$

$$\chi_v = h_m \frac{1}{V_a^2 k_v^m} + h_b \frac{1}{V_a^2 k_v^b} \tag{32}$$

The diffusivity of Xe atoms was taken from recent atomistic calculations [23, 30]. For stoichiometric U_3Si_2, Xe diffusivity is assumed to be dominated by transport in the *aa* direction of the unit cell (as described in Ref. [23]), and diffusivity is given by $D_g = D_1 + D_3$. D_1 is the thermal diffusivity and is given by $D_1 = D_0 \exp \frac{-E_m}{k_B T}$, where $D_0 = 2.85 \times 10^{-4}$ m^2/s and $E_m = 3.17$ eV. D_3 is the athermal diffusivity, a measure of effective diffusion from radiation damage-induced ballistic mixing, and is given by $D_3 = 3.58 \times 10^{-42} \dot{F}$ [30]. At the simulation temperature of 1035 K, thermal diffusivity dominates, and $D_g = 0.1$ nm^2/s. The rate of vacancy transport to fission gas bubbles is influenced by the balance between the rate of vacancy production, s_v^0, and the diffusion coefficient of vacancies, D_v. Since s_v^0 is not well known and we are using an assumed value, we further assume that the diffusivity of vacancies is the same as that of gas atoms: $D_v = D_g$. The much larger value of s_v^0 ensures that a large supply of

vacancies is available and therefore gas bubble growth is limited by the supply of gas atoms, consistent with the typical assumptions of bubble growth during steady-state reactor operating conditions [21].

In order to optimize the performance of the PetSC nonlinear solver used in the numerical solution of the problem for each time step, the governing equations were non-dimensionalized so that all problem quantities are of order unity, using length scale $l^* = 1$ nm, time scale $\tau^* = 0.1$ s, and energy density scale $E^* = 63 \times 10^9$ J/m^3. Finally, we describe the parameterization of the order parameter mobility L. In the simulation configuration used, the grain boundary between fuel matrix grains is static, and the change in microstructure is only due to the motion of matrix-bubble interfaces. We assume the motion of the matrix-bubble interfaces is diffusion-limited, and set the non-dimensionalized order parameter mobility $\bar{L}$ large enough that further increases do not change the observed microstructural evolution. This ensures that the motion of the matrix-bubble interface is diffusion controlled. Using this approach, we set $\bar{L} = 1$, which is equivalent to a dimensional value $L = \frac{\bar{L}}{E^* \tau^*} = 1.59 \times 10^{-10}$ m^3/(J s). The physical parameters used for phase-field simulations are summarized in Table 1.

The non-dimensionalized governing equations were discretized using the MOOSE framework [31]. Hexahedral 3D mesh elements with linear Lagrange shape functions were used for spatial discretization. Mesh adaptivity was used, with three levels of refinement and a minimum element size of $\Delta x = \Delta y = \Delta z = 10$ nm so that the element size in the interfacial regions is 1/3 of the interfacial width ($l_{int} = 30$ nm). No-flux boundary conditions were used in all directions. The second-order backward differentiation formula was used for time integration, and adaptive time stepping was used as implemented in the MOOSE IterationAdaptiveDT time stepper [32].

Parameter	Value
T	1035 K
V_a	0.03629 nm^3
E_v^f	1.69 eV
E_v^g	4.92 eV
$c_g^{b,eq}$	0.3924
$c_v^{b,eq}$	0.6076
$k_v^m = k_g^m$	5.28×10^{11} J/m^3
$k_v^b = k_g^b$	8.0×10^{10} J/m^3
f_0	1.82×10^9 J/m^3
κ	1.92×10^{-8} J/m
m	6.84×10^8 J/m^3
γ_{mib0}	1.5
γ_{mimj}	0.6749
$\dot{F}$	1.26×10^{13} fissions/(cm^3 s)
Y_{Xe}	0.2156
s_g^0	2.72×10^{12} atoms/(cm^3 s)
s_v^0	2.72×10^{13} vacancies/(cm^3 s)
D_g	0.1 nm^2/s
D_v	0.1 nm^2/s
L	1.59×10^{-10} $\text{m}^3/(\text{J s})$

Table 1: Parameters used for phase-field simulations.

3. Phase-Field Simulations

3.1. Simulation initial conditions

To investigate the growth of the intergranular bubbles, a planar bicrystal geometry with lenticular bubbles placed on the grain boundary was used for the simulation initial conditions. An example of the initial conditions is shown in Figure 1a. The simulation domain size in the x, y, and z directions was L_x, L_y, and L_z, respectively, where $L_x = 480$ nm, $L_y = L_z = 2960$ nm. The grain boundary is located at $x = L_x/2 = 240$ nm. The grain located at $x < 240$ nm is represented by order parameter η_{m1}, and the grain located at $x > 240$ nm is represented by order parameter η_{m2}.

The bubbles are represented by the order parameter η_{b0}. In the initial conditions, N lenticular bubbles with semi-dihedral angle $\theta/2 = 73°$ [14] are placed at random locations on the grain boundary with a minimum center-to-center distance between bubbles l_{min}. The initial radius of the bubbles' circular projection onto the grain boundary is 61 nm such that the initial bubble diameter is several times larger than the interfacial width of the phase-field model. The number of bubbles is determined by $N = n_a A$, where n_a is the areal density of bubbles and A is the area of the grain boundary. Due to the important effect of n_a shown in Ref. [19], an accurate value must be determined for use in the simulation initial conditions. To do so, the rate theory simulations of Ref. [2] were used. Assuming a truncated octahedron grain geometry with a volume equal to that of a 5 μm diameter spherical grain, the surface area of the space-filling truncated octahedron is $A_{TO} = 86.3$ μm^2 and its volume $V_{TO} = 65.4$ μm^3. From Ref. [2], the number density of grain boundary bubbles n_v at 1035 K is 10^{13} cm^{-3} at 45 GWD/tU. The areal density can be computed from $n_a = \frac{V_{TO} n_v}{A_{TO}/2} = 15.2$ μm^{-2} (where the factor of 2 accounts for the fact that each grain boundary is shared with an adjacent truncated octahedron). Although some concentration of gas atoms and vacancies would have built up in the fuel matrix far from the grain boundary at 45 GWD/tU, diffusional transport of defects to the grain boundary bubbles leads to a region depleted of defect species near the grain boundary. Be-

cause of the relatively small size of the simulation domain in the x-direction, we assume the matrix phase in the simulation domain lies in this depleted region and therefore has a negligible defect concentration in the initial conditions.

3.2. Simulation results

An example of the simulated microstructural evolution is shown in Fig. 1. For this simulation, $T = 1035$ K, $\theta/2 = 73°$, $n_a = 15/\mu\text{m}^2$, $l_{min} = 160$ nm. The lenticular bubbles in the initial conditions are shown in Fig. 1a. In Fig. 1b, the bubbles have grown, and some bubbles have begun to interconnect with one another. In Fig. 1c, many of the bubbles are interconnected with each other, and most (but not all) of the bubbles are connected to the edge of the simulation domain. At a simulation time of 1.97×10^8 s, all the bubbles have connected to one of the edges of the simulation domain; the microstructure at that time is shown in Fig. 1d.

To determine the progress of release of gas from the bubbles, the grain boundary coverage and the fraction of bubbles that are assumed to be vented is calculated by analyzing the phase-field simulation results at each time step. The grain boundary coverage X_{GB}^C is calculated as the fraction of area on the grain boundary where $\eta_{b0} > 0.5$. To calculate the fraction of bubbles that are vented, it is assumed that when a bubble comes into contact with edge of the grain boundary (edge of the simulation domain), it connects to a triple junction network at the edge of that grain boundary (which is not represented explicitly in the simulation), and that the gas within the bubble can then be vented from the fuel. The fraction of bubbles that are vented, X_{GB}^V, is calculated as the area on the grain boundary that is covered by bubbles that are connected to the edge of the grain boundary divided by the total area covered by the bubble phase.

Figure 2a shows the progress of X_{GB}^C and X_{GB}^V versus time for the simulation shown in Figure 1. The increase in both quantities with respect to time is much less rapid than observed in Ref. [19] because vacancies and gas atoms build up slowly from the source terms in the present work, as opposed to existing in the initial conditions as a high initial supersaturation of defects as in Ref. [19]. The

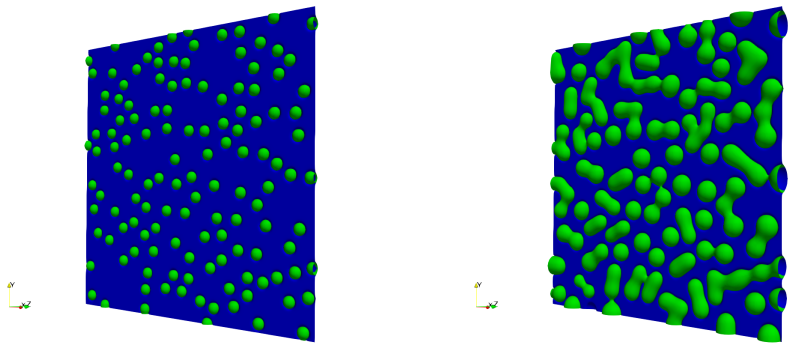

(a) Initial conditions

(b) $t = 6.04 \times 10^7$ s

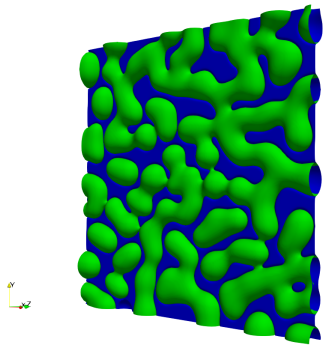

(c) $t = 1.62 \times 10^8$ s

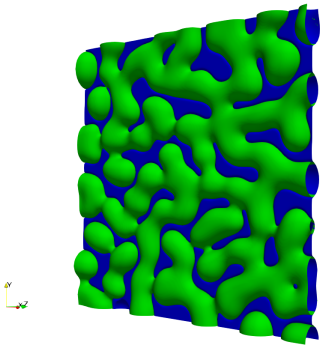

(d) $t = 1.97 \times 10^8$ s

Figure 1: Evolution of microstructure during simulated growth of grain boundary bubbles in U_3Si_2. The grain boundary is shown in blue and the gas bubbles are shown in green. Simulation temperature T = 1035 K, $\theta/2 = 73°$, $n_a = 15/\mu m^2$, $l_{min} = 160$ nm. At $t = 1.97 \times 10^8$ s, all bubbles have connected to the edge of the simulation domain.

areal density of bubbles n_a is shown as a function of time in Fig. 2b. No bubble coalescence occurs in the early stages of the plot due to the minimum initial spacing l_{min} imposed in the initial conditions. Once bubble coalescence begins, the rate of bubble coalescence is relatively constant until the bubble density reaches approximately half its initial value, after which the rate of coalescence decreases.

In Figure 2c, X_{GB}^V is plotted as a function of X_{GB}^C for the simulation shown in Fig. 1. The rate of venting is relatively slow until $X_{GB}^C > 0.5$ and increases rapidly until $X_{GB}^C \approx 0.6$; at that point, the rate of venting slows down until venting completes at $X_{GB}^C = 0.74$. These results are consistent with the trends observed in Ref. [19].

3.2.1. Determination of engineering-scale model parameters from simulation results

From these simulations, an estimate of $F_{c,sat}$ can be determined for input to the engineering-scale fuel performance code BISON. As discussed in Section 1, the BISON model assumes that when the grain boundary coverage reaches $F_{c,sat}$, all the bubbles simultaneously interconnect with each other and release their gas to the free space between the fuel and cladding. On a plot of X_{GB}^V versus X_{GB}^C as in Fig. 2c, this would be represented by a step function, with $X_{GB}^V = 0$ for $X_{GB}^C < F_{c,sat}$ and $X_{GB}^V = 1$ for $X_{GB}^C \geq F_{c,sat}$. In Ref. [12], the theoretical value $F_{c,sat} = 0.78$ was used. To determine an improved estimate from the phase-field simulations, we assume that $F_{c,sat}$ occurs when the slope of the curve in Fig. 2c is maximum, as this best approximates the step function behavior used in the BISON model. Using this assumption, for the plot in Fig. 2c, $F_{c,sat} = 0.62$. With this definition, for this example more than 80% of bubble area is vented when $F_c = F_{c,sat}$.

3.2.2. Effect of simulation assumptions and parameters on calculated $F_{c,sat}$

In this section, key assumptions involved in the simulations of Section 3.2 are considered to determine their effect on the calculated engineering-scale model

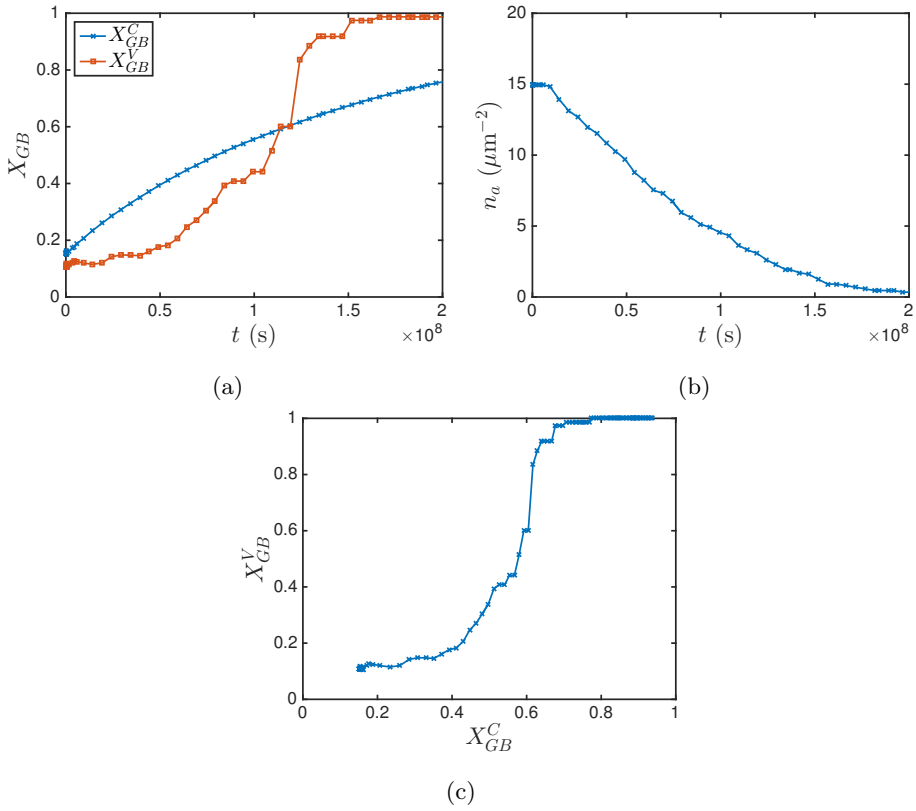

Figure 2: (a) Fractional grain boundary coverage, X_{GB}^C, and fraction of grain boundary bubbles that are vented, X_{GB}^V, versus time, for the simulation shown in Figure 1. (b) Areal density of grain boundary bubbles, n_a, plotted versus time. (c) Plot of fraction of grain boundary bubbles that are vented, X_{GB}^V, as a function of fractional coverage of the grain boundary by bubbles, X_{GB}^C.

parameter $F_{c,sat}$ and to quantify the uncertainty in this calculated parameter.

In physical fuel samples, each grain boundary contains randomly positioned grain boundary bubbles with areal density n_a. Because of the random positioning of the bubbles on the grain boundary, the curve shown in Fig. 2c is expected to be different for each grain boundary, resulting in a different calculated $F_{c,sat}$. To determine the effect of the variation in initial bubble positions on the calculated value of $F_{c,sat}$, 4 additional simulations with the same parameters as shown in Fig. 1 were run, but with a different seed in the random number generator used to produce the initial bubble positions along the grain boundary. Thus, the set of (y, z) positions of the bubble centers in the initial conditions were different for each of the 5 simulations, but the x position of each bubble remained $L_x/2$ for each bubble in all simulations. All other simulation parameters and initial conditions remained the same between the 5 simulations. From these simulations, plots of X_{GB}^V versus X_{GB}^C were produced, and $F_{c,sat}$ was calculated for each simulation. The results of these calculations are shown in Table 2. The mean value of $F_{c,sat}$ was determined to be 0.60 from this set of simulations, with a standard deviation of 0.036. (Although more than five samples should ideally be considered when determining statistical quantities such as the standard deviation, computational resource limitations prevented considering a larger number of samples.) The relatively small standard deviation indicates that the calculated value of $F_{c,sat}$ is relatively insensitive to the initial bubble position distribution.

The next assumption considered is the minimum spacing between bubbles in the simulation initial conditions, l_{min}. Although the rate theory simulations used to set the initial conditions allow determination of n_a, they do not contain information about the spacing between bubbles; therefore they cannot be used to determine a value for l_{min}. Since the correct value for this parameter is unknown, a set of simulations was conducted to determine how important its effect is on the rate of venting and the value of $F_{c,sat}$ calculated for input to BISON simulations. Plots of X_{GB}^V versus X_{GB}^C for varying l_{min} are shown in Fig. 3. For $l_{min} = 130$ nm, the early stages of release are similar to $l_{min} = 160$

Configuration	$F_{c,sat}$
1	0.54
2	0.62
3	0.61
4	0.63
5	0.62
Mean	**0.60**
Standard Deviation	**0.036**

Table 2: Variation in calculated engineering-scale model parameter $F_{c,sat}$ for varying initial grain boundary bubble positions. For this set of simulations, the parameters used are the same as those for the simulations shown in Fig. 1, and only the random positions of the bubbles in the initial conditions are varied.

nm. However, the majority of the gas release occurs slightly later, and the value of $F_{c,sat}$ determined is increased to 0.65 for this set of initial conditions. For a larger value of $l_{min} = 200$ nm, the early stages of gas release are delayed relative to the $l_{min} = 130$ nm and $l_{min} = 160$ nm cases. This is because the larger initial spacing on average delays connections between bubbles until X_{GB}^C is larger. However, once interconnection begins for the $l_{min} = 200$ nm case, the rate of interconnection is more rapid in the range $0.5 < X_{GB}^C < 0.6$. This is because the initial bubbles are closer to evenly spaced, so once they grow enough to begin interconnecting, interconnection occurs more rapidly.

To better quantify the effect of varying l_{min} on $F_{c,sat}$, a set of 5 total simulations with different initial random bubble positions were run for the $l_{min} = 130$ nm and $l_{min} = 200$ nm cases, similar to the $l_{min} = 160$ nm case. For the $l_{min} = 130$ nm simulations, $F_{c,sat} = 0.61 \pm 0.039$, while for the $l_{min} = 200$ nm simulations, $F_{c,sat} = 0.58 \pm 0.046$. Thus, recalling that for $l_{min} = 160$ nm, $F_{c,sat} = 0.60 \pm 0.036$, there is a trend of a slight decrease in the mean calculated value of $F_{c,sat}$ with increase in l_{min}. This is consistent with the observations of the data shown in Fig. 3 and discussion in the previous paragraph. However, the

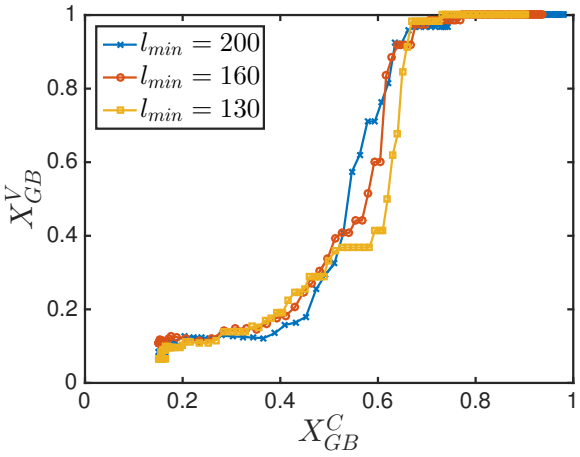

Figure 3: Effect of varying l_{min} on grain boundary saturation behavior. For a smaller $l_{min} =$ 130 nm, $F_{c,sat}$ is delayed to 0.65. For a larger $l_{min} = 200$ nm, in the earlier stages of venting ($X_{GB}^C < 0.5$) venting is delayed compared to the smaller l_{min} cases, but the rate of increase is more rapid in the range $0.5 < X_{GB}^C < 0.6$.

total variation of $F_{c,sat}$ is smaller than the standard deviation of each calculated value, so the trend may be merely the result of statistical variation.

The next assumption considered is the simulated grain boundary geometry. For a given grain boundary area, the shape of the grain boundary used in the simulation affects the length of the perimeter of the simulation domain. Because it is assumed that the gas bubbles must connect to the perimeter of the grain boundary to connect to a triple junction that would provide a pathway for gas escape, it is possible that the length of the perimeter could affect the rate of venting. Grain growth simulations in 3D have shown that the average number of edges per grain boundary is greater than 5 [33], so the 4-sided grain boundary used in the present simulations may underestimate the actual rate of venting. To test the effect of grain boundary geometry, we consider the extreme case of a circular grain boundary, which has the maximum perimeter length for a fixed grain boundary area, and compare the results of venting to the square grain boundary geometry.

A set of 5 simulations with a circular grain boundary with the same area and

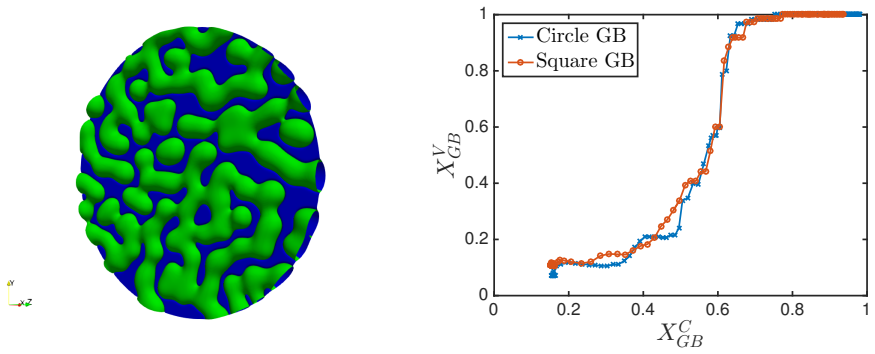

(a) $t = 1.61 \times 10^8$ s (b)

Figure 4: (a) Gas bubble microstructure of circular grain boundary with same simulation parameters as those shown in Fig. 1c, at approximately the same time. (b) Comparison of X^V_{GB} versus X^C_{GB} for the square and circular grain boundary geometries. The similarity of the results indicates that the grain boundary geometry does not strongly affect the progress toward venting of the gas bubbles.

number of bubbles as the previously used square grain boundary was conducted, with $l_{min} = 160$ nm and other simulation parameters remaining the same as used in the square grain boundary simulations. An example of the microstructure of the gas bubbles in one of these simulations is shown in Fig. 4a, at approximately the same time as the microstructure shown in Fig. 1c. Plots of X^V_{GB} versus X^C_{GB} for one example of the circular and square grain boundaries are shown in Fig. 4b. Although some differences are observed, overall the shapes of the curves are quite similar. An average value of $F_{c,sat} = 0.61 \pm 0.046$ was calculated from the 5 simulations of circular grain boundaries, which is very close to the average value predicted for the square grain boundary of the same area and value of l_{min}, which was $F_{c,sat} = 0.60 \pm 0.036$. Based on these simulations, we conclude that the geometry of the grain boundary in the simulations does not have a significant effect on the qualitative behavior of venting or the calculated value of $F_{c,sat}$.

The final assumption considered is the simulation temperature. The current BISON model of fission gas release and swelling in U_3Si_2 uses a constant

value of $F_{c,sat}$ that does not vary with temperature. The phase-field model used in this work was used to provide insight into whether this is a valid assumption. The simulations described so far were conducted at a temperature of 1035 K, which is representative of the temperature at the center of a fuel pellet at relatively high power. Changes in temperature have the potential to impact many of the parameters used in the phase-field model; however, the impact of temperature on the parameters that have been shown to be important in the progress of venting [19] is quite small. The average grain boundary energy and average bubble-matrix interfacial energy is nearly constant with temperature over the range of temperatures relevant to LWR operation [14], approximately 700K - 1100K. Similarly, the areal density of grain boundary bubbles in the initial conditions determined from simulations is nearly constant over the same range [2].

In the present system, the main simulation parameter that is expected to be strongly impacted by changing temperature is the diffusivity of the defect species. To demonstrate the effect of temperature variation and corresponding defect diffusivity on microstructural evolution, simulations were conducted at $T = 1015$ K and 1084 K, with corresponding defect diffusivities $D_v = D_g = 0.05$ nm^2/s and 0.5 nm^2/s, respectively, based on atomistic calculations [23, 30]. All other parameters remained as in Table 1, and $l_{min} = 160$ nm.

As seen in Figure 5, the microstructure is strongly affected by the changes to the defect diffusion coefficient. Higher diffusivities result in a less interconnected microstructure and larger feature sizes with smaller average curvatures for equal simulation times. This is because a higher diffusion coefficient allows the process of coarsening, which is a driving force to reduce interfacial area and average curvature, to proceed with faster kinetics. To evaluate the effect of the change in diffusivities on the progress of the gas bubbles toward venting, a set of 5 simulations with $D_v = D_g = 0.05$ nm^2/s was conducted, corresponding to $T = 1015$ K. From these simulations, an average value of $F_{c,sat} = 0.60 \pm 0.014$ was calculated. So, in spite of the changes in microstructure, the calculated value of $F_{c,sat}$ was not affected, although the time needed to reach that value

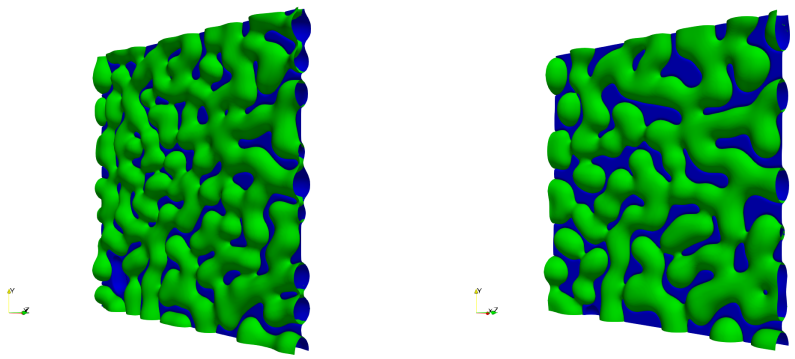

(a) $D_v = D_g = 0.05$ nm^2/s

(b) $D_v = D_g = 0.1$ nm^2/s

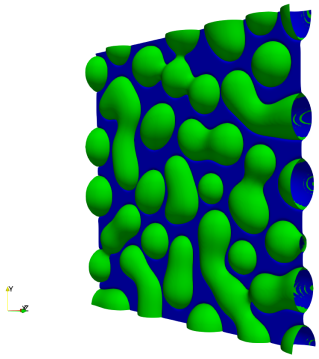

(c) $D_v = D_g = 0.5$ nm^2/s

Figure 5: Effect of defect diffusivity on microstructure. Microstructures are shown at time $t = 1.97 \times 10^8$ s. (a) $D_v = D_g = 0.05$ nm^2/s, (b) $D_v = D_g = 0.1$ nm^2/s, (c) $D_v = D_g = 0.5$ nm^2/s.

of $F_{c,sat}$ is increased.

Because portions of the fuel are expected to be at $T < 1015$ K, diffusivities in those portions of the fuel are expected to be lower than the range considered in these simulations. We did attempt to conduct simulations at temperatures lower than 1015 K; however, because of the slower diffusivities, defect concentration increased significantly in the matrix where they are deposited by the source terms, resulting in formation of intragranular fission gas bubbles. Because the model is parametrized to simulate intergranular bubbles, the interface width is much larger than the expected physical size of the intragranular bubbles, and the intragranular bubbles that formed were much larger than the nm-sized bubbles expected in intragranular regions. Therefore, we did not attempt to calculate $F_{c,sat}$ from these simulations since they do not represent expected physical behavior because of the model parametrization and limitations of the diffuse interface approach. In summary, we conclude that the calculated value of $F_{c,sat}$ is unaffected by temperature over the range we were able to consider, but allow that behavior may differ outside that range. Future advances in model formulation and computing power may allow simultaneous consideration of the intergranular and intragranular bubbles with realistic sizes.

3.2.3. Comparison with past theoretical and computational results

In this section, we compare the results obtained in our simulations with previous theoretical and computational studies conducted on similar systems. The value of $F_{c,sat}$ obtained here, 0.60, is significantly lower than the value obtained for a uniform square lattice, 0.78 [18], which is expected based on the uniform lattice's more efficient packing. However, the randomly positioned bubbles in the present simulations more realistically approximate the expected gas bubble microstructure in a fuel pellet.

Significant past effort has been given to determining the percolation threshold of various geometries. In the present context, the percolation threshold p_c is the grain boundary bubble area fraction at which a path through the bubble phase exists that spans across the entire grain boundary. For a uniform lattice,

because all bubbles intersect simultaneously, $F_{c,sat} = p_c$. However, in general p_c should not necessarily be expected to be exactly the same as $F_{c,sat}$ for randomly positioned bubbles. Comparison with 2D percolation results are most relevant, since percolation in our simulations occurs in the 2D grain boundary plane. The percolation threshold of randomly positioned overlapping circles was determined to be 0.6764 when the circle radii were uniform, and 0.6860 when the radii were non-uniform [34]. A closer approximation to the microstructure obtained in our simulations was found in Ref. [35], which considered the nucleation and growth of precipitates from a supersaturated matrix phase in 2D. In that work, the percolation threshold was determined to be 0.661 (although those results may differ depending on the simulation parameters used and the amount of time the simulation is allowed to run). Thus, the value of $F_{c,sat}$ determined in the present simulations (and observed experimentally in UO_2 [16]) is below the value of p_c determined for the most comparable 2D geometries. This may be due to the fact that the existence of a bubble spanning across the entire grain boundary is not required for all bubbles to connect to a grain edge and thus for the criteria to reach $F_{c,sat}$ to be met. It may also partially result from the assumptions made in calculating $F_{c,sat}$.

The present simulation results can also be compared to the results of Millett et al. for bubble growth by post-irradiation annealing in UO_2. Although $F_{c,sat}$ was not calculated in Ref. [19], it appears from the plots of X_{GB}^V vs. X_{GB}^C in that work that similar results would be obtained. This, combined with the consistent values of $F_{c,sat}$ obtained for different diffusion coefficients in the present work, suggests that the value of $F_{c,sat} = 0.60$ may be a general result for interconnecting grain boundary bubbles, and not specific to the choice of material parameters or growth mechanism.

4. Conclusions

To provide mechanistic insights and calculate necessary parameters for engineering-scale modeling of U_3Si_2 fuel, a phase-field model of intergranular fission gas

bubble growth was parametrized using atomistic and rate theory simulations, and simulations of the growth of bubbles on a grain boundary were performed. The grain boundary coverage and fraction of bubbles that were vented to the edge of the domain were plotted versus time to characterize the progress of venting. The progress of these quantities versus time was much slower than previous simulations in UO_2 fuel, due to the fact that the UO_2 fuel simulations used an initial supersaturation of gas atoms in the initial conditions and were thus more representative of post-irradiation annealing. When the fraction of vented bubbles was plotted versus the grain boundary coverage by bubbles, the results were similar to the previous UO_2 simulations. (However, $F_{c,sat}$ was not calculated from the UO_2 simulations, so only qualitative comparisons are possible.)

From the phase-field simulation results, the parameter $F_{c,sat}$ (saturation coverage of grain boundaries) for the current BISON fuel performance model was determined. For the nominal set of simulation parameters, $F_{c,sat} = 0.60 \pm 0.036$, calculated from the $F_{c,sat}$ for 5 configurations of randomly placed initial bubble positions. The effect of important model assumptions and uncertain simulation parameters on the calculated value of $F_{c,sat}$ was considered. Larger values for l_{min}, the initial spacing between bubbles, resulted in a small decrease in the calculated $F_{c,sat}$; however, the trend may be only the result of statistical variation. The geometry of the grain boundary in the simulations was found to not have a significant effect on the calculated value of $F_{c,sat}$. Simulation temperature was also found to not have a significant effect on the calculated value of $F_{c,sat}$, although it did affect the microstructure. However, the range of temperatures considered does not cover the full range of temperatures that would be experienced by U_2Si_2 fuel due to limitations of the current model parametrization.

The phase-field simulations described in this work also provide insight for future improvements to the engineering-scale swelling and fission gas release model described in Ref. [12]. The simulations show that gas release occurs over a range of values of grain boundary coverage, rather than with a rapid step

function change at a single value as the current model assumes. Therefore, future work in BISON should focus on incorporating a gradual release of gas according to curves calculated by Marmot simulations, but only after a percolated triple junction network is formed [15].

Acknowledgments

This work was funded by the Department of Energy Nuclear Energy Advanced Modeling and Simulation program and the Consortium for Advanced Simulation of Light Water Reactors. This manuscript has been authored by Battelle Energy Alliance, LLC under Contract No. DE-AC07-05ID14517 with the US Department of Energy. Los Alamos National Laboratory, an affirmative action/equal opportunity employer, is operated by Triad National Security, LLC, for the National Nuclear Security Administration of the U.S. Department of Energy under Contract No. 89233218CNA000001. The United States Government retains and the publisher, by accepting the article for publication, acknowledges that the United States Government retains a nonexclusive, paid-up, irrevocable, world-wide license to publish or reproduce the published form of this manuscript, or allow others to do so, for United States Government purposes.

Data availability

The raw/processed data required to reproduce these findings cannot be shared at this time due to legal reasons.

References

[1] J. T. White, A. T. Nelson, J. T. Dunwoody, D. D. Byler, D. J. Safarik, and K. J. McClellan. Thermophysical properties of U_3Si_2 to 1773 K. *Journal of Nuclear Materials*, 464:275–280, 2015.

[2] Y. B. Miao, K. A. Gamble, D. Andersson, B. Ye, Z. G. Mei, G. Hofman, and A. M. Yacout. Gaseous swelling of U_3Si_2 during steady-state LWR operation: A rate theory investigation. *Nuclear Engineering and Design*, 322:336–344, 2017.

[3] Y. B. Miao, K. A. Gamble, D. Andersson, Z. G. Mei, and A. M. Yacout. Rate theory scenarios study on fission gas behavior of U_3Si_2 under LOCA conditions in LWRs. *Nuclear Engineering and Design*, 326:371–382, 2018.

[4] M. R. Finlay, G. L. Hofman, and J. L. Snelgrove. Irradiation behaviour of uranium silicide compounds. *Journal of Nuclear Materials*, 325:118–128, 2004.

[5] Y. B. Miao, J. Harp, K. Mo, S. Bhattacharya, P. Baldo, and A. M. Yacout. Short communication on "in-situ TEM ion irradiation investigations on U_3Si_2 at LWR temperatures". *Journal of Nuclear Materials*, 484:168–173, 2017.

[6] Y. B. Miao, J. Harp, K. Mo, S. F. Zhu, T. K. Yao, J. Lian, and A. M. Yacout. Bubble morphology in U_3Si_2 implanted by high-energy Xe ions at 300 degrees C. *Journal of Nuclear Materials*, 495:146–153, 2017.

[7] Y. B. Miao, J. Harp, K. Mo, Y. S. Kim, S. F. Zhu, and A. M. Yacout. Microstructure investigations of U_3Si_2 implanted by high-energy Xe ions at 600 degrees C. *Journal of Nuclear Materials*, 503:314–322, 2018.

[8] T. K. Yao, B. W. Gong, L. F. He, J. Harp, M. Tonks, and J. Lian. Radiation-induced grain subdivision and bubble formation in U_3Si_2 at LWR temperature. *Journal of Nuclear Materials*, 498:169–175, 2018.

[9] T. K. Yao, B. W. Gong, L. F. He, Y. B. Miao, J. M. Harp, M. Tonks, and J. Lian. In-situ TEM study of the ion irradiation behavior of U_3Si_2 and U_3Si_5. *Journal of Nuclear Materials*, 511:56–63, 2018.

[10] H. Shimizu. The properties and irradiation behavior of U_3Si_2. Technical Report NAA-SR-10621, Atomics International, 1965.

[11] J. Rest. A model for fission-gas-bubble behavior in amorphous uranium silicide compounds. *Journal of Nuclear Materials*, 325(2-3):107–117, 2004.

[12] T. Barani, G. Pastore, D. Pizzocri, D. A. Andersson, C. Matthews, A. Alfonsi, K. A. Gamble, P. Van Uffelen, L. Luzzi, and J. D. Hales. Multiscale modeling of fission gas behavior in U_3Si_2 under LWR conditions. *Journal of Nuclear Materials*, 522:97–110, 2019.

[13] G. Pastore, L. Luzzi, V. Di Marcello, and P. Van Uffelen. Physics-based modelling of fission gas swelling and release in UO_2 applied to integral fuel rod analysis. *Nucl. Engrg. Design*, 256:75 –86, 2013.

[14] B. Beeler, M. Baskes, D. Andersson, M. W. D. Cooper, and Y. F. Zhang. Molecular dynamics investigation of grain boundaries and surfaces in U_3Si_2. *Journal of Nuclear Materials*, 514:290–298, 2019.

[15] L. K. Aagesen, D. Schwen, M. R. Tonks, and Y. F. Zhang. Phase-field modeling of fission gas bubble growth on grain boundaries and triple junctions in UO_2 nuclear fuel. *Computational Materials Science*, 161:35–45, 2019.

[16] R.J.White. The development of grain-face porosity in irradiated oxide fuel. *Journal of Nuclear Materials*, 325:61 –77, 2004.

[17] G. Pastore, L.P. Swiler, J.D. Hales, S.R. Novascone, D.M. Perez, B.W. Spencer, L. Luzzi, P. Van Uffelen, and R.L.Williamson. Uncertainty and sensitivity analysis of fission gas behavior in engineering - scale fuel modeling. *Journal of Nuclear Materials*, 456:398 –408, 2015.

[18] T. Kogai. Modelling of fission gas release and gaseous swelling of light water reactor fuels. *Journal of Nuclear Materials*, 244:131–140, 1997.

[19] P. C. Millett, M. R. Tonks, S. B. Biner, L. Z. Zhang, K. Chockalingam, and Y. F. Zhang. Phase-field simulation of intergranular bubble growth and percolation in bicrystals. *Journal of Nuclear Materials*, 425(1-3):130–135, 2012.

[20] M. R. Tonks, D. Gaston, P. C. Millett, D. Andrs, and P. Talbot. An object-oriented finite element framework for multiphysics phase field simulations. *Computational Materials Science*, 51:20–29, 2012.

[21] D.R.Olander. *Fundamental aspects of nuclear reactor fuel elements.* Technical Information Center, Energy Research and Development Administration, 1976.

[22] N. Moelans. A quantitative and thermodynamically consistent phase-field interpolation function for multi-phase systems. *Acta Materialia*, 59(3):1077–1086, 2011.

[23] D. A. Andersson, X. Y. Liu, B. Beeler, S. C. Middleburgh, A. Claisse, and C. R. Stanek. Density functional theory calculations of self- and Xe diffusion in U_3Si_2. *Journal of Nuclear Materials*, 515:312–325, 2019.

[24] Yulan Li, Shenyang Hu, Robert Montgomery, Fei Gao, and Xin Sun. Phase-field simulations of intragranular fission gas bubble evolution in UO_2 under post-irradiation thermal annealing. *Nuclear Instruments and Methods in Physics Research Section B: Beam Interactions with Materials and Atoms*, 303:62–67, 2013.

[25] C. Kittel and H. Kroemer. *Thermal Physics.* W. H. Freeman and Company, 1980.

[26] N. Moelans, B. Blanpain, and P. Wollants. Quantitative analysis of grain boundary properties in a generalized phase field model for grain growth in anisotropic systems. *Phys. Rev. B*, 78:024113, 2008.

[27] http://nele.studentenweb.org/docs/parameters.m; accessed 07-Oct-2017.

[28] International Atomic Energy Agency. Chain fission yields. https://www-nds.iaea.org/sgnucdat/c1.htm; accessed 13-Apr-2017.

[29] M. Plapp. Unified derivation of phase-field models for alloy solidification from a grand-potential functional. *Physical Review E*, 84(3):031601, 2011.

[30] M. W. D. Cooper, C. Matthews, C. R. Stanek, D. A. Andersson, K. Gamble, B. W. Beeler, and G. Pastore. Fission gas and creep in uranium silicide fuel. Report L3:FMC.FUEL.P19.05, Los Alamos National Laboratory, 2019.

[31] D. Gaston, C. Newman, G. Hansen, and D. Lebrun-Grandié. MOOSE: A parallel computational framework for coupled systems of nonlinear equations. *Nuclear Engineering and Design*, 239:1768–1778, 2009.

[32] J. D. Hales, K. A. Gamble, B. W. Spencer, S. R. Novascone, G. Pastore, W. Liu, D. S. Stafford, R. L. Williamson, D. M. Perez, and R. J. Gardner. BISON users manual. Technical Report INL/MIS-13-30307, Rev. 3, Idaho National Laboratory, September 2015.

[33] J. K. Mason, E. A. Lazar, R. D. MacPherson, and D. J. Srolovitz. Geometric and topological properties of the canonical grain-growth microstructure. *Physical Review E*, 92(6), 2015.

[34] B. Lorenz, I. Orgzall, and H.-O. Heuer. Universality and cluster structures in continuum models of percolation with two different radius distributions. *Journal of Physics A: Mathematical and General*, 26:4711–4722, 1993.

[35] V. E. Brunini, C. A. Schuh, and W. C. Carter. Percolation of diffusionally evolved two-phase systems. *Physical Review E*, 83:021119, 2011.